ELSEVIER

Journal of Fluids and Structures 19 (2004) 369–386

JOURNAL OF FLUIDS AND STRUCTURES

www.elsevier.nl/locate/jnlabr/yjfls

A numerical study of flow-induced noise in a two-dimensional centrifugal pump. Part II. Hydroacoustics

M.A. Langthjem*, N. Olhoff

Institute of Mechanical Engineering, Aalborg University, Pontoppidanstræde 101, DK-9220 Aalborg East, Denmark

Received 23 December 2003; accepted 12 January 2004

Abstract

This paper is concerned with determination of the acoustic pressure field in a centrifugal pump. The main noise-generating mechanism is assumed to be the unsteady impeller blade surface forces, which reach a maximum when the flow channel between two consecutive blades is shut off by the volute tongue. The acoustic sources are moving (rotating) dipoles. The strengths of these dipoles are estimated by using the discrete vortex method described in Part I of this two-part study, but may be determined by any other (appropriate) flow analysis method. The solution to the inhomogeneous wave equation which describes the generation and propagation of pressure waves is expressed in the frequency domain, by making use of Fourier transform. The dipole-type boundary term, which accounts for the scattering from the volute, is discretized by employing the boundary element method. The emphasis is on a two-dimensional procedure, but extension to three dimensions is also discussed. The method is applied to the flat 'two-dimensional' laboratory centrifugal pump considered in Part I. The frequency-domain solution is particularly useful for this kind of problem, as the interest typically is in the dominating frequency components only, which are the blade passage frequency f_{blade} and its higher harmonics, $2f_{\text{blade}}$, $3f_{\text{blade}}$, etc. The numerical results are compared with available experimental results, by which they are well supported. The frequency-domain solution is also found to be very useful in connection with minimization of the flow-noise by design optimization.

1. Introduction

Centrifugal pumps are widely used for transporting fluids though pipe systems, not only in industrial environments but also in home and office appliances, such as heating and cooling systems, water supply, etc. It is thus important that the fluid transport is accompanied with as little noise as possible. Flow-induced noise in a centrifugal pump is mainly generated by blade–tongue interaction (Chu et al., 1995; Dong et al., 1997). When a couple of impeller blades pass by the tongue, the fluid channel between them is gradually blocked, resulting in generation of a pressure pulse. These pulses are transmitted throughout the pipe system as sound waves. As these waves are subject to very little frictional attenuation, they may cause annoying noise and vibrations far away from the source (Lighthill, 1978).

For flows characterized by a small Mach number,

$$M = \frac{\text{Characteristic flow speed}}{\text{Speed of sound}} = \frac{U}{c_0}, \tag{1}$$

*Corresponding author. Present address: Department of Mechanical Systems Engineering, Faculty of Engineering, Yamagata University, 4-3-16 Jonan, Yonezawa, Yamagata 992-8510, Japan. Tel.: +81-238-26-3326; fax: +81-238-26-3205.

E-mail address: mikael@yz.yamagata-u.ac.jp (M.A. Langthjem).

0889-9746/$ - see front matter © 2004 Elsevier Ltd. All rights reserved.
doi:10.1016/j.jfluidstructs.2004.01.002

Nomenclature

c_0	speed of sound
$c(\mathbf{x})$	geometric coefficient, defined by (11)
d_j	design parameters
f	frequency
f_{blade}	blade passage frequency, $\Omega N_{\text{blades}}/2\pi$
$\mathbf{f}$	rotating point force
F	dipole forcing term
$\mathscr{F}$	volute design curve (B-spline)
G	Green's function
H	Heaviside function, $H(x)=1$ for $x>0$ and 0 for $x<0$
$\mathrm{H}_v^{(1)}$	Hankel function of first kind and order v
i	Complex unit, $\sqrt{-1}$
$\mathbf{I}$	Unit matrix
J	number of sampled force/pressure values, see (26), (27)
J_v	Bessel function of first kind and order v
k	acoustic wavenumber, ω/c_0
n, $\mathbf{n}$	normal vector
N_{blades}	number of impeller blades
N_e	number of boundary elements
N_f	number of rotating forces
N_{nodes}	number of nodes in each boundary element
p	acoustic pressure
p_0	reference pressure
$\mathbf{q}_0$	vector of rotating dipoles (frequency domain)
r	distance from source located at $\mathbf{y}$ to point of observation $\mathbf{x}$
R_T	impeller outer radius
$\mathbf{S}_0$	element matrix, see (30)
t	time
U	characteristic flow speed
U_T	rotor peripheral velocity, $R_T\Omega$
$\mathbf{x}$	point of observation
$\mathbf{y}$	source location
Y_v	Bessel function of second kind and order v

Greek symbols

δ	Dirac delta function, $\int_{-\infty}^{\infty}\delta(x)\,\mathrm{d}x=1$, $\delta(x)=0$ for $x\neq 0$
ρ_0	fluid density
τ	source time parameter
ϕ_n	boundary element shape function
ω	radian frequency, $2\pi f$
Ω	angular velocity

the generation and propagation of sound waves in a fluid may be represented by an inhomogeneous wave equation on the form

$$\underbrace{\frac{\partial^2 p}{\partial t^2}-c_0^2\nabla^2 p}_{\text{propagation}}=\underbrace{c_0^2 s(\mathbf{x},t)}_{\text{source}}, \tag{2}$$

where $p(\mathbf{x},t)$ is the fluid pressure at position $\mathbf{x}=(x_1,x_2)$ (or (x_1,x_2,x_3) in three dimensions) and at time t, c_0 is the speed of sound, ∇^2 is the Laplacian, and the source term $s(\mathbf{x},t)$ is a sound-generating forcing function which may be written as

$$s(\mathbf{x},t)=\frac{\partial Q}{\partial t}-\frac{\partial F_i}{\partial x_i}-\frac{\partial^2 T_{ij}}{\partial x_i \partial x_j} \tag{3}$$

(Howe, 1998), where summation over repeated indices is to be applied. The scalar function Q represents simple sources, the vector function F_i represents unsteady pressure forces, and the tensor function T_{ij} represents a stress distribution due to turbulent velocity- and pressure-fluctuations. The terms correspond, from left to right, to monopole, dipole, and quadrupole sources, respectively. The monopole is the most efficient source, generating pressure pulsations proportional to U^2 in the three-dimensional far field. The dipole generates pressure pulsations proportional to U^3, while those generated from the quadrupole are proportional to U^4. The acoustic power generated is thus proportional to U^4 for the monopole, U^6 for the dipole, and U^8 for the quadrupole (Guelich and Bolleter, 1992). In a two-dimensional model, as considered in this paper, the pressures are proportional to $U^{3/2}$, $U^{5/2}$, and $U^{7/2}$, respectively, giving acoustic powers proportional to U^3, U^5, and U^7 (Guo, 2000).

Monopole sources may exist in a centrifugal pump in form of nonuniform outflow from the impeller, and in the form of flow and stagnation pressure oscillations at the pump discharge. But these are normally weak in a well-designed pump. Dipole sources exist in the form of fluctuating pressure forces on both rotating and stationary parts. These may be of significant magnitude, especially for pumps with high hydrodynamic efficiencies. Quadrupole sources are found in the unsteady, highly turbulent wake flow. Ffowcs Williams and Hawkings (1969a) analyzed the balance between dipole and quadrupole contributions to the total sound generation by multi-bladed fans rotating in a free field, and showed that the quadrupole contribution may be comparable with the dipole contribution if the fan has very many blades rotating near sonic speed ($M \approx 1.0$). But for a typical centrifugal pump, with 5–10 blades running at $M \approx 0.01$ (which is a typical value), the noise contribution from quadrupoles can safely be neglected (Howe, 1991).

A second dipole-type sound source in turbomachines is the 'chopping' of vortices when they are squeezed in between the volute tongue and the trailing edges of the impeller blades, and then cut by the blades. If U_T is the peripheral impeller blade velocity and r_v is the radius of a vortex core, the characteristic frequency of the vortex chopping noise is approximately U_T/r_v (Howe, 1991). This is much higher than the characteristic frequency of the oscillating surface forces, which are the blade passage frequency, $f_{\text{blade}} = U_T N_{\text{blades}}/(2\pi R_T)$, and its harmonics, $2f_{\text{blade}}$, $3f_{\text{blade}}$, …, where N_{blades} is the number of impeller blades and R_T is the impeller radius. Experiments show that the dominating pressure signals in centrifugal pumps are at the blade passage frequency and the first 4–5 harmonics (Guelich and Bolleter, 1992; Chu et al., 1995; Rzentkowski, 1996; Dong et al., 1997). Vortex chopping noise is therefore ignored in the present paper.

The discrete vortex method is applied to give the unsteady velocity field, as described in Part I (Langthjem and Olhoff, 2003). Once the velocities are known, the forces exerted on the impeller blades are evaluated from the unsteady Bernoulli equation. In the present approach the distributed blade forces are 'lumped' into point forces, acting at specified control points. The sound generation in a fluid by direct excitation of a fluctuating point force was discussed by Lighthill (1952). That paper was mainly concerned with the noise generation by turbulent fluid motion, and laid the foundation to *aeroacoustics*. The influence of solid boundaries was investigated by Curle (1955). Point forces in rectilinear motion was discussed by Lighthill (1962). Lowson (1965) developed the theory for point forces in arbitrary, subsonic motion. These results were extended to surfaces moving with arbitrary velocities by Ffowcs Williams and Hawkings (1969b). Their general result, the so-called Ffowcs Williams and Hawkings (FW–H) equation, has been successful in predicting the noise generated by the blades of rotating machinery, such as helicopter rotors, see Farassat and Brentner (1998).

The foundation work cited above was formulated for three-dimensional problems. Only recently, the FW–H equation was reformulated in a two-dimensional setting. This was done simultaneously but independently by Lockard (2000) and by Guo (2000). Their work is discussed further in Section 7.

The 'lumping' of the distributed, unsteady surface pressure fluctuations into a number of fluctuating point forces can be thought of as a simple discretization of the FW–H equation. This formulation was chosen for its simplicity. Jeon and Lee (1999) used the discrete vortex method (in two-dimensional formulation, as used in the present paper) to evaluate the unsteady flow generated by a centrifugal fan rotating in the vicinity of a wedge. Following this, the acoustic pressure fluctuations were evaluated by using Lowson's result (in three-dimensional formulation) and ignoring the scattering by the wedge. Scattering from a closed casing was considered in Jeon and Lee (2000).

The theory described in this paper is kept in a two-dimensional formulation throughout. This is done in order to include the scattering effects of the pump casing in the simplest way. Applying the theory to a basically two-dimensional laboratory pump, such as the one used by Chu et al. (1995), the essential features of the noise generation within the pump will likely be captured, although the amplitude of the sound waves may be overestimated. However, the necessary modifications to extend the analysis to three dimensions are also discussed.

The paper is organized as follows. Section 2 describes assumptions regarding the mathematical model, the governing, inhomogeneous wave equation, and its solution in integral representation. The discretization of this equation is described in Section 3. Section 4 is concerning with some relative simple test problems, used to verify individual parts of the numerical scheme. In Section 5, calculations of the acoustic pressure in a centrifugal pump are presented and compared with experimental results. Section 6 discusses use of the developed analysis method in connection with

minimization of the flow-induced noise by shape-optimization of the tongue. The conclusions are summarized in Section 7.

2. The sound field

2.1. Description of the mathematical model

Consider the 'two-dimensional' laboratory pump sketched in Fig. 1(a). To estimate the noise generated by the flow in the pump, the following assumptions are made.

(i) The rotational Mach number $M_r = U_T/c_0 \ll 1$. As an example, an impeller with diameter 25 cm running in water at 1000 r.p.m. has $M_r \approx 0.01$, assuming that the speed of sound $c_0 = 1400$ m s^{-1}.
(ii) Monopole sources (due to nonuniform outflow from the impeller) and quadrupole sources (due to turbulent velocity and pressure fluctuations) are much weaker than the dipole sources (due to surface pressure fluctuations), and can be neglected.
(iii) Both the incompressible 'background' flow field and the acoustic field are two-dimensional.
(iv) Acoustic pressure fluctuations do not have significant influence (back-reaction) on the 'background' flow.
(v) The pump casing (volute) and the exit channel are completely rigid.

The noise sources are assumed, then, to be the unsteady, rotating fluid forces acting on the impeller blades, as sketched in Fig. 1(b). These forces are, for the time being, assumed known. [They are specified later, by (14).] Thus the acoustic pressure $p(\mathbf{x}, t)$ at the observation point $\mathbf{x} = (x_1, x_2)$ can be obtained from the linear wave equation with a sound-generating dipole-type forcing term included on the right-hand side, as follows:

$$\frac{\partial^2 p}{\partial t^2} - c_0^2 \nabla^2 p = F(\mathbf{x}, t), \tag{4}$$

where the dipole term F is given by

$$F(\mathbf{x}, t) = -c_0^2 \sum_{j=1}^{N_{\text{blades}}} \boldsymbol{\nabla} \cdot \{\mathbf{F}(\mathbf{y}_j(t), t)\delta(\mathbf{x} - \mathbf{y}_j(t))\}. \tag{5}$$

Here $\boldsymbol{\nabla}\cdot$ is the divergence operator (see also (3)),

$$\mathbf{F}(\mathbf{y}_j(t), t) = (F_1(\mathbf{y}_j(t), t), F_2(\mathbf{y}_j(t), t))$$

are fluid forces per unit volume acting on the rotating impeller blades, δ is the Dirac delta function, and

$$\mathbf{y}_j(t) = (y_1(t), y_2(t))_j = |\mathbf{y}_j|(\cos(\Omega t), -\sin(\Omega t)) \tag{6}$$

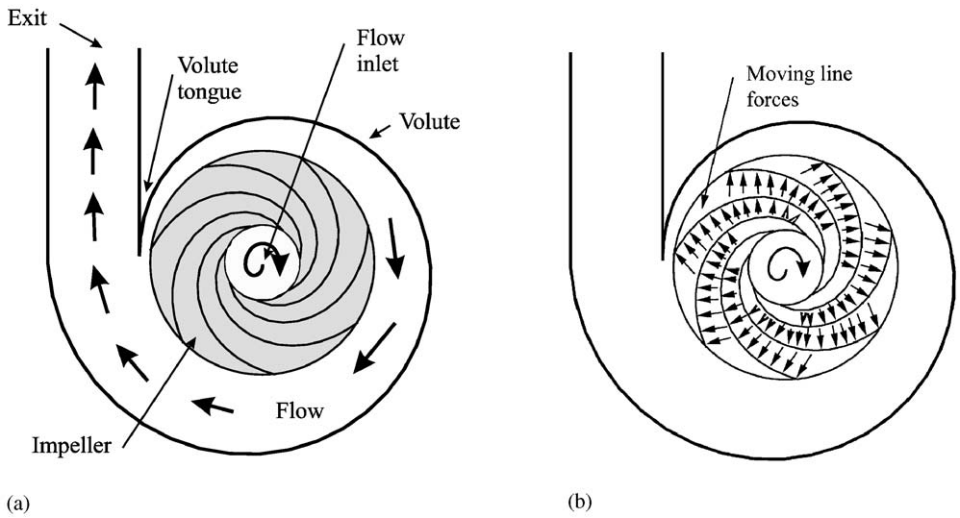

Fig. 1. (a) Schematic of a volute-type centrifugal pump, (b) acoustic model.

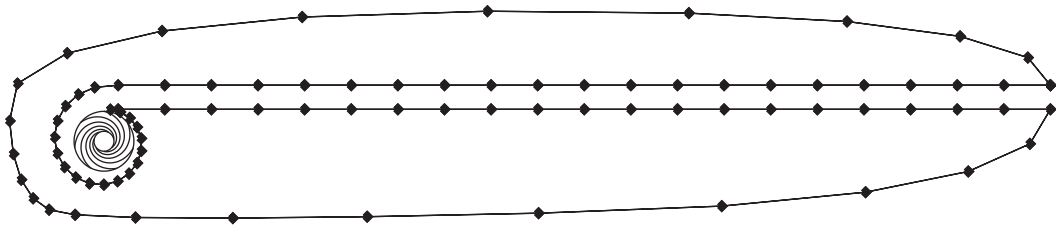

Fig. 2. Complete acoustic computational model, illustrating the distribution of boundary elements.

are points on the impeller blade surfaces at time t, presuming that the impeller rotates in the clockwise direction. The somewhat lengthy notation is employed to emphasize that the forces are not stationary in space, but rotate with the angular velocity Ω. The influence of viscosity on the pressure waves is known to be insignificant (Lighthill, 1978) and is also ignored here.

With the assumption of a completely rigid pump casing and exit channel (see Fig. 2), the boundary condition to be satisfied everywhere on the surface is

$$\frac{\partial p}{\partial \mathrm{n}} = 0, \tag{7}$$

where $\partial/\partial n$ symbolizes the derivative in the direction of the normal vector $\mathbf{n}$ which points *into* the enclosure. Considering each impeller blade as a closed surface, the same boundary condition applies to these moving boundaries since, again, the influence of the mean flow on the acoustic pressure can be ignored. But the impeller blades will not be represented by moving surfaces. They will, ultimately, be represented just by a number of moving line forces. It may seem, then, that the impeller blades will be transparent to the acoustic pressure waves. It will be shown later in this section, however, that (7) is satisfied on the impeller blades exactly at the positions where the line forces attack. This is analogous to the flow analysis (Part I), where the impeller blades are represented by just a number of line vortices, and where the boundary condition of zero normal velocity is satisfied only at control points slightly off-set from the line vortices. In the numerical analysis the impeller blades then satisfy (7) just as 'well' as the casing, since this condition cannot be enforced numerically *everywhere* on the casing boundary, but only at a limited number of control points (see Section 3.2).

2.2. Solution of the inhomogeneous wave equation

In order to solve Eq. (4) (with (7) imposed) we consider the wave equation

$$\frac{\partial^2 G}{\partial t^2} - c_0^2 \nabla^2 G = \delta(\mathbf{x} - \mathbf{y})\delta(t - \tau), \tag{8}$$

where $\mathbf{y} = (y_1, y_2)$ are source coordinates, and τ a source time coordinate. The right-hand side represents an impulsive point source placed at $\mathbf{y}$ and working only at time $t = \tau$. The two-dimensional, free-space Green function G satisfying this equation, and having outgoing wave behavior, is given by (Howe, 1998)

$$G(\mathbf{x}, \mathbf{y}, t, \tau) = \frac{H(c_0(t - \tau) - r)}{2\pi c_0 \sqrt{c_0^2 (t - \tau)^2 - r^2}}. \tag{9}$$

Here $H(s)$ is the Heaviside function, which takes the value 1 for $s > 0$ and 0 for $s < 0$, and $r = |\mathbf{x} - \mathbf{y}|$. Considering the denominator of (9), it is seen that G represents an outgoing cylindrical wave with a slowly decaying 'tail'. This is different from the three-dimensional case, where the corresponding Green's function is an impulsive, outgoing wave (without any tail).

By using (8), the solution to (4) is obtained as

$$c(\mathbf{x}) p(\mathbf{x}, t) = \int_\tau \int_{\mathbf{y}} c_0^2 \{FG + (G\nabla^2 p - p\nabla^2 G)\} \, \mathrm{d}^2\mathbf{y} \, \mathrm{d}\tau, \tag{10}$$

where the integration is performed over the entire source plane ('pump area') $\mathbf{y}$ ($-\infty < y_1, y_2 < \infty$) and over all source times τ ($-\infty < \tau < \infty$). The coefficient

$$c(\mathbf{x}) = \begin{cases} 1 & \text{if } \mathbf{x} \text{ is in the interior of the acoustic medium,} \\ \frac{1}{2} & \text{if } \mathbf{x} \text{ is on the boundary,} \\ 0 & \text{if } \mathbf{x} \text{ is outside the acoustic medium.} \end{cases} \tag{11}$$

In three dimensions, $c(\mathbf{x})$ represents the solid angle of the bounding surface, seen from the point $\mathbf{x}$. This is 4π away from the boundary and 2π on the boundary, provided that there is a unique tangent plane there, and zero inside the bounding surface. The result (11), sometimes referred to as Green's 3rd identity (Hansen, 1991), also holds in two dimensions; here the angle is 2π away from the boundary and π on the boundary. In this way the factor $\frac{1}{2}$ appears. A mathematical proof of (11) can be found in, e.g., Chen and Zhou (1992).

Considering the first term in (10), the divergence operator can, by integration by parts, be transferred to the Green function G, as follows:

$$\begin{aligned} &-\sum_{j=1}^{N_{\text{blades}}} \int_\tau \int_{\mathbf{y}} c_0^2 \nabla \cdot \{\mathbf{F}(\mathbf{y}_j(\tau), \tau)\delta(\mathbf{x} - \mathbf{y}_j(\tau))\} G \, \mathrm{d}^2\mathbf{y} \, \mathrm{d}\tau \\ &= \sum_{j=1}^{N_{\text{blades}}} \int_\tau \int_{\mathbf{y}} c_0^2 \{\mathbf{F}(\mathbf{y}_j(\tau), \tau)\delta(\mathbf{x} - \mathbf{y}_j(\tau))\} \cdot \frac{\partial G}{\partial \mathbf{y}} \, \mathrm{d}^2\mathbf{y} \, \mathrm{d}\tau, \end{aligned} \tag{12}$$

where $\partial G/\partial \mathbf{y} = (\partial G/\partial y_1, \partial G/\partial y_2)$. The boundary terms vanish as there are no dipoles placed at $y_1, y_2 = \pm\infty$. Carrying out the integration over $y_1$and y_2 (i.e., over all blade surfaces), (12) reduces to

$$\sum_{n=1}^{N_f} \int_\tau c_0^2 \mathbf{f}_n(\mathbf{y}_n(\tau), \tau) \cdot \frac{\partial G}{\partial \mathbf{y}} \, \mathrm{d}\tau, \tag{13}$$

where $\mathbf{f}_n$ are 'lumped' line forces (force per unit breadth) which act on the impeller blade control points $\mathbf{y}_n(t)$ (as specified in Part I, Fig. 3). These forces are obtained as

$$\mathbf{f}_n(\mathbf{y}_n(t), t) = \mathbf{n}_n(\mathbf{y}_n(t))\Delta p_n \ell_n, \quad n = 1, 2, \ldots, N_f, \;\; N_f = N_{bv} N_{\text{blades}}. \tag{14}$$

Here N_{bv} is the number of bound vortices on each impeller blade, $\mathbf{n}_n(\mathbf{y}_n(t))$ is the normal vector at $\mathbf{y}_n(t)$, Δp_n is the hydrodynamic pressure difference across blade control point n (obtained from an incompressible flow analysis, see Part I, Eq. (16)), and ℓ_n is the length of vortex panel n.

Green's theorem gives the second and third terms in (10) as

$$c_0^2 \int_\tau \int_{\mathbf{y}} \{G\nabla^2 p - p\nabla^2 G\} \, \mathrm{d}^2\mathbf{y} \, \mathrm{d}\tau = c_0^2 \int_\tau \oint_s \left\{ p_s \frac{\partial G}{\partial \mathrm{n}} - G \frac{\partial p_s}{\partial \mathrm{n}} \right\} \mathrm{d}s \, \mathrm{d}\tau, \tag{15}$$

where $\oint_s \mathrm{d}s$ refers to integration around the closed boundary curve, and p_s is the pressure acting on the boundary. The boundary condition (7) gives that the second term is equal to zero.

In order to bring the formal solution (10) into a form suitable for numerical evaluation, it is most convenient to express the Green function (9) in terms of its Fourier transform, given by (Howe, 1998)

$$G(\mathbf{x}, \mathbf{y}, t, \tau) = \frac{\mathrm{i}}{8\pi c_0^2} \int_\omega \mathrm{H}_0^{(1)}(kr(\tau))\mathrm{e}^{-\mathrm{i}\omega t}\mathrm{e}^{\mathrm{i}\omega\tau} \, \mathrm{d}\omega, \tag{16}$$

where $\mathrm{H}_0^{(1)}$ is the Hankel function of first kind and zeroth order (Abramowitz and Stegun, 1972), $r(\tau) = |\mathbf{x} - \mathbf{y}(\tau)|$, ω is the frequency parameter, $k = \omega/c_0$ is the wavenumber, and $\mathrm{i} = \sqrt{-1}$. The Hankel function $\mathrm{H}_0^{(1)}$ represents an outgoing cylindrical wave, as may been seen by considering its approximation for large arguments (see (22) in the next subsection).

Eq. (10) can now be written as

$$\begin{aligned} c(\mathbf{x})p(\mathbf{x}, t) = &\sum_{n=1}^{N_f} \int_\tau \mathbf{f}_n(\mathbf{y}_n(\tau), \tau) \frac{\partial}{\partial \mathbf{y}} \cdot \left[\frac{\mathrm{i}}{8\pi} \int_\omega \mathrm{H}_0^{(1)}(kr_n(\tau))\mathrm{e}^{-\mathrm{i}\omega t} \, \mathrm{e}^{\mathrm{i}\omega\tau} \, \mathrm{d}\omega \right] \mathrm{d}\tau \\ &+ \int_\tau \oint_s p(\mathbf{y}_s, \tau) \frac{\partial}{\partial \mathrm{n}} \left[\frac{\mathrm{i}}{8\pi} \int_\omega \mathrm{H}_0^{(1)}(kr_s)\mathrm{e}^{-\mathrm{i}\omega t} \, \mathrm{e}^{\mathrm{i}\omega\tau} \, \mathrm{d}\omega \right] \mathrm{d}s \, \mathrm{d}\tau, \end{aligned} \tag{17}$$

where $\mathbf{y}_s$ denotes coordinates along the boundary.

By defining the Fourier transform of the pressure as

$$p(\mathbf{x},\omega)=\int_t p(\mathbf{x},t)\mathrm{e}^{\mathrm{i}\omega t}\,\mathrm{d}t,\quad p(\mathbf{x},t)=\frac{1}{2\pi}\int_\omega p(\mathbf{x},\omega)\mathrm{e}^{-\mathrm{i}\omega t}\,\mathrm{d}\omega, \tag{18}$$

Eq. (17) can be expressed in the frequency domain as

$$\begin{aligned}c(\mathbf{x})p(\mathbf{x},\omega)=&\frac{\mathrm{i}}{4}\sum_{n=1}^{N_f}\int_\tau \mathbf{f}_n(\mathbf{y}_n(\tau),\tau)\cdot\frac{\partial}{\partial\mathbf{y}}\mathrm{H}_0^{(1)}(kr_n(\tau))\mathrm{e}^{\mathrm{i}\omega\tau}\,\mathrm{d}\tau\\&+\frac{\mathrm{i}}{4}\int_\tau\oint_s p(\mathbf{y}_s,\tau)\frac{\partial}{\partial\mathrm{n}}\mathrm{H}_0^{(1)}(kr_s)\mathrm{e}^{\mathrm{i}\omega\tau}\,\mathrm{d}s\,\mathrm{d}\tau.\end{aligned} \tag{19}$$

Using (18) again, the second (boundary) term can be written as

$$\frac{\mathrm{i}}{4}\oint_s p(\mathbf{y}_s,\omega)\frac{\partial}{\partial\mathrm{n}}\mathrm{H}_0^{(1)}(k_jr_s)\,\mathrm{d}s. \tag{20}$$

It is noticed that the two terms in (19) have the same form. In particular, the directions of the line forces $\mathbf{f}_n$ are normal to the impeller blades and thus, $\partial\mathrm{H}_0^{(1)}/\partial\mathbf{y}$ in the first line could just as well be written as $\partial\mathrm{H}_0^{(1)}/\partial\mathrm{n}$. This means that the boundary condition (7) is satisfied at the positions where the rotating point forces attack, as mentioned earlier. Furthermore, (19) shows that the influence from the casing also corresponds to a distribution of dipoles, a continuous distribution rather than a number of concentrated ones, as for the impeller blades. But by discretization of the second term in (19) (for numerical analysis, see Section 3.2), the continuous dipole distribution on the casing will, in a way, be 'lumped' into discrete dipoles. At that stage the two terms in (19) become equivalent. [Change of the solution (19) to one valid in three dimensions is described in Appendix A.]

Finally, it is useful to list in this Section the derivatives of the Hankel function; these are given by

$$\begin{aligned}\frac{\partial}{\partial y_\alpha}\mathrm{H}_0^{(1)}(k_jr_n(t))&=k_j\mathrm{H}_1^{(1)}(k_jr_n(t))\frac{x_\alpha-y_{\alpha n}(t)}{r_n(t)},\\\frac{\partial}{\partial\mathrm{n}}\mathrm{H}_0^{(1)}(k_jr_s)&=k_j\mathrm{H}_1^{(1)}(k_jr_s)\frac{(\mathbf{x}-\mathbf{y}_s)\cdot\mathbf{n}}{r_s},\end{aligned} \tag{21}$$

since $\partial\mathrm{H}_\nu^{(1)}/\partial z=-\mathrm{H}_{\nu+1}^{(1)}(z)+\nu\mathrm{H}_\nu^{(1)}(z)/z$ and $\partial r/\partial y_\alpha=-(x_\alpha-y_\alpha)/r$. These results explicitly display the characteristic dipole directivity. Consider, for example, a harmonically oscillating line force $\mathbf{f}=(f(\omega),0)$ acting at $\mathbf{y}=(0,0)$ in the x_1 direction, in a free field. Putting $x_1=r\cos\theta$ the resulting pressure (19) is equal to $p=\frac{\mathrm{i}}{4}fk\mathrm{H}_1^{(1)}(kr)\cos(\theta)$. At large distances from the force the acoustic particle radial velocity $u_r=p/\rho_0c_0$. The acoustic intensity, defined as $I=pu_r$ (Lighthill, 1978), then takes the value $I=-\{fk\mathrm{H}_1^{(1)}(kr)\}^2\cos^2(\theta)/16\rho_0c_0$. The factor $\cos^2(\theta)$ gives the well-known figure of eight-shaped directivity.

2.3. Sound pressure far away from the pump

In the 'near field', very near the noise sources themselves, $kr\ll1$, and $k\mathrm{H}_1^{(1)}(kr)\sim-\mathrm{i}/(2\pi r)$. Eq. (19) then shows that $p(\mathbf{x},\omega)\sim U^2$, since $\mathbf{f}_n(\mathbf{y}_n(\tau),\tau)$ and $p(\mathbf{y}_s,\tau)$ are proportional to U^2, according to the Bernoulli equation. In contrast, in the 'far field', where the point of observation $\mathbf{x}$ is far away from the noise sources, $|\mathbf{x}|\gg|\mathbf{y}|$ and $kr\gg1$. Then

$$\mathrm{H}_1^{(1)}(kr)\sim-\mathrm{i}\sqrt{\frac{2}{\pi kr}}\mathrm{e}^{\mathrm{i}(kr-\pi/4)},\quad r\sim|\mathbf{x}|-\frac{\mathbf{x}\cdot\mathbf{y}}{|\mathbf{x}|}\ \text{ and }\ \frac{1}{r}\sim\frac{1}{|\mathbf{x}|}. \tag{22}$$

Inserting (21) and (22) into (19) gives

$$\begin{aligned}c(\mathbf{x})p(\mathbf{x},\omega)\sim&\sum_{n=1}^{N_f}\int_\tau k\frac{\mathbf{x}}{|\mathbf{x}|}\cdot\mathbf{f}_n(\mathbf{y}_n(\tau),\tau)\sqrt{\frac{1}{8\pi\mathrm{i}k|\mathbf{x}|}}\mathrm{e}^{\mathrm{i}\omega\tau}\mathrm{e}^{\mathrm{i}k|\mathbf{x}|}\mathrm{e}^{-\mathrm{i}k\mathbf{x}\cdot\mathbf{y}_n(\tau)/|\mathbf{x}|}\,\mathrm{d}\tau\\&+\oint_s k\frac{\mathbf{x}}{|\mathbf{x}|}\cdot\mathbf{n}\,p(\mathbf{y}_s,\omega)\sqrt{\frac{1}{8\pi\mathrm{i}k|\mathbf{x}|}}\mathrm{e}^{\mathrm{i}k|\mathbf{x}|}\mathrm{e}^{-\mathrm{i}k\mathbf{x}\cdot\mathbf{y}_s/|\mathbf{x}|}\,\mathrm{d}s,\end{aligned} \tag{23}$$

which by ignoring the now small changes in the force positions $\mathbf{y}_n(\tau)$ (as seen from $\mathbf{x}$) may be further simplified to

$$c(\mathbf{x})p(\mathbf{x},\omega)\sim \sum_{n=1}^{N_f} k\frac{\mathbf{x}}{|\mathbf{x}|}\cdot\mathbf{f}_n(\mathbf{y}_0,\omega)\sqrt{\frac{1}{8\pi ik|\mathbf{x}|}}\mathrm{e}^{\mathrm{i}k|\mathbf{x}|}\mathrm{e}^{-\mathrm{i}k\mathbf{x}\cdot\mathbf{y}_0/|\mathbf{x}|} + \oint_s k\frac{\mathbf{x}}{|\mathbf{x}|}\cdot\mathbf{n}p(\mathbf{y}_s,\omega)\sqrt{\frac{1}{8\pi ik|\mathbf{x}|}}\mathrm{e}^{\mathrm{i}k|\mathbf{x}|}\mathrm{e}^{-\mathrm{i}k\mathbf{x}\cdot\mathbf{y}_s/|\mathbf{x}|}\,\mathrm{d}s, \tag{24}$$

assuming that $\mathbf{y}_n(\tau)\approx\mathbf{y}_0$, the 'mean position' of all N_f forces. The terms $\mathbf{f}_n(\mathbf{y}_0,\omega)$ and $p(\mathbf{y}_s,\omega)$ are still proportional to U^2, while purely complex terms (with phase angle 90° ahead of displacements) are proportional to U. It then follows from (24) that

$$p(\mathbf{x},t)\sim U^{5/2} \tag{25}$$

as also showed by Guo (2000).

3. Discretization

3.1. Discrete Fourier transform

In correspondence with (18) the discrete Fourier transform of the pressure is defined by

$$p(\mathbf{x},\omega_j)=\sum_{k=0}^{J-1}p(\mathbf{x},t_k)\mathrm{e}^{\mathrm{i}\omega_j t_k},\quad p(\mathbf{x},t_k)=\frac{1}{J}\sum_{j=0}^{J-1}p(\mathbf{x},\omega_j)\mathrm{e}^{-\mathrm{i}\omega_j t_k}. \tag{26}$$

The discrete version of (19) then takes the form

$$c(\mathbf{x})p(\mathbf{x},\omega_j)=\frac{\mathrm{i}}{4}\sum_{k=0}^{J-1}\sum_{n=1}^{N_f}\mathbf{f}_n(\mathbf{y}_n(t_k),t_k)\cdot\frac{\partial}{\partial\mathbf{y}}\mathrm{H}_0^{(1)}(k_j r_n(t_k))\mathrm{e}^{\mathrm{i}\omega_j t_k} + \frac{\mathrm{i}}{4}\oint_s p(\mathbf{y}_s,\omega_j)\frac{\partial}{\partial\mathrm{n}}\mathrm{H}_0^{(1)}(k_j r_s)\,\mathrm{d}s,\quad j=0,1,2,\ldots,J-1. \tag{27}$$

In order to make the frequency composants more 'sharp', the first term is multiplied by a modified Hann window function (Press et al., 1992), similar to the one suggested by Lockard (2000). The window function is a Hann window at the first and last $\frac{1}{8}$ parts, and a square window at the middle $\frac{3}{4}$ part.

Eq. (27) is particularly useful for numerical evaluation if the interest is only in a few frequency components of the pressure, for example, the blade passage frequency f_{blade} and a number of the higher harmonics, $2f_{\mathrm{blade}}, 3f_{\mathrm{blade}}, \ldots$, say. This is the typical situation in connection with centrifugal pumps.

3.2. Discretization of the boundary integral

The boundary integral in (27) is evaluated numerically by using the boundary element method (BEM) (Crighton et al., 1992). The boundary is discretized into N_e elements. Within each element, the pressure is represented by

$$p(\mathbf{y}_e)=\sum_{n=1}^{N_{\mathrm{nodes}}}\phi_n(\mathbf{y}_e)p_e^n, \tag{28}$$

where N_{nodes} is the number of nodes in each elements, and ϕ_n are shape functions. In two-dimensional analyses, one, two, or three nodes are typically used, corresponding to constant pressure, linear varying pressure, and quadratic varying pressure, respectively, within each element. Using (28), the boundary integral is approximated by

$$\oint_s p(\mathbf{y}_s)\frac{\partial}{\partial\mathrm{n}}\mathrm{H}_0^{(1)}(k_j r_s)\,\mathrm{d}s\approx\sum_{e=1}^{N_e}\sum_{n=1}^{N_{\mathrm{nodes}}}p_e^n\int_{s_e}\phi_n(\mathbf{y}_e)\frac{\partial}{\partial\mathrm{n}}\mathrm{H}_0^{(1)}(k_j(r_e))\,\mathrm{d}s_e, \tag{29}$$

where r_e is the distance from nodal point e to the observation point $\mathbf{x}$. Using (27) and (29) the pressure is evaluated at each element nodal point in turn. This gives a set of linear equations with the same number of unknown nodal pressures. The equation system can be written as

$$[\tfrac{1}{2}\mathbf{I}-\mathbf{S}_0]\mathbf{p}_s=\mathbf{q}_0, \tag{30}$$

where $\mathbf{I}$ is the unit matrix. The element S_{ij} in the matrix $\mathbf{S}_0$ is the scattered pressure at nodal point i due to a unit pressure acting on element j. The vector $\mathbf{q}_0$ contains the pressures from the rotating dipoles, evaluated at the element nodal points. After having solved (30) with respect to $\mathbf{p}_s$, the pressure at a point $\mathbf{x}_*$ is obtained as

$$p(\mathbf{x}_*) = \mathbf{s}_*^{\mathrm{T}}\mathbf{p}_s + \mathbf{q}_*, \tag{31}$$

where $\mathbf{s}_*$ is a vector of influence coefficients, and $\mathbf{q}_*$ corresponds to $\mathbf{q}_0$, but evaluated at $\mathbf{x}_*$.

The simplest possible boundary element, i.e. with $N_{\mathrm{nodes}} = 1$, is found to be sufficient for the present work. The integrals are evaluated by Gauss–Legendre quadrature, using ten points (Press et al., 1992). The boundary elements are connected to the same B-spline nodal points as used for the volute source panels in the discrete vortex method, see Section 2 in Part I. The two uppermost exit pipe panels are connected to each other via an element-covered outer boundary curve (see Fig. 2), such that the complete boundary is a closed curve, as assumed in Green's theorem (see (10) and (15)). Alternatively, to avoid the outer boundary, special 'thin body' panels, which constitute closed surfaces in themselves, could be used (Wu and Wan, 1992; Jeon and Lee, 2000).

The equation system (30) is solved by LU-decomposition. The Hankel functions $\mathrm{H}_\nu^{(1)}$ are evaluated by application of library routines for the Bessel functions J_ν and Y_ν, using that $\mathrm{H}_\nu^{(1)}(z) = \mathrm{J}_\nu(z) + \mathrm{i}\mathrm{Y}_\nu(z)$. In particular, for real x,

$$\mathrm{H}_\nu^{(1)}(x) = \{\mathrm{sgn}(x)\}^{\nu+1}\mathrm{J}_\nu(|x|) + \mathrm{i}\{\mathrm{sgn}(x)\}^{\nu}\mathrm{Y}_\nu(|x|). \tag{32}$$

But only $\nu = 1$ needs to be considered for the present case.

4. Verification of individual parts in the numerical method

Some relatively simple problems which admit analytical solutions have been considered to validate the individual parts in the numerical method. The implementation of the BEM into a Fortran 90 computer program was validated by calculating the scattering of a plane sound wave by a cylinder, and comparing with the analytical results of Morse and Ingard (1986). Let a denote the radius of the cylinder, and $k = \omega/c_0$ the wave number. The incoming pressure wave is travelling in the direction of the positive x-axis, and is given by

$$p = p_0 \mathrm{e}^{\mathrm{i}k(x-c_0 t)}. \tag{33}$$

Polar diagrams, showing the absolute value of the surface pressure for various values of ka, are depicted in Figs. 3(a)–(c). Parts (d)–(f) show the pressures at the distance $r = 5a$ from the center of the cylinder. In all BEM calculations, the surface was discretized into 100 elements. The accuracy is decreasing with increasing values of ka. But considering that kr is small in the centrifugal pump problem,[1] these examples indicate that the use of constant pressure elements is sufficient. [See also the discussion in Section 5.2.]

The implementation of the isolated dipole terms was validated by considering the sound pressure generated from a single discrete vortex element, of length 2 m, having the oscillating line force placed at $\mathbf{y} = (0.5\ \mathrm{m}, 0.0)$ and the control point at $(-0.5\ \mathrm{m}, 0.0)$. The line force of magnitude 1 N m^{-1} is oscillating with the frequency $f = 20$ Hz, see Fig. 4(a). Eq. (19) gives the pressure as

$$p(\mathbf{x}, \omega) = \frac{\mathrm{i}}{4}(0,1)\cdot k\mathrm{H}_1^{(1)}(kr)\frac{\mathbf{x} - (0.5, 0.0)}{r} \quad (\mathrm{Pa}). \tag{34}$$

The wavenumber $k = 2\pi f/c_0 = 0.08976$ m^{-1}, assuming $c_0 = 1400$ m s^{-1}. At $x = (0.5\ \mathrm{m}, 1.0\ \mathrm{m})$, corresponding to $r = 1$ m, $\mathrm{H}_1^{(1)}(kr) = 0.04483 + \mathrm{i}7.1788$, giving a pressure amplitude of $p = 0.1611$ Pa. The program gives this value as well, as seen from Fig. 4(b).

5. Calculations of acoustic pressure in a centrifugal pump

5.1. Description of tongue geometries and location of calculation points

The method described in Sections 2 and 3 will be applied to the pump considered in Section 4 in Part I of the paper. Three different volute tongues will be considered. They resemble tongues 1–3 in Dong et al. (1997). See Fig. 5 for a sketch. Tongue 1 has a gap of 7% of the impeller radius, while the gaps of Tongues 2 and 3 are 11% and 18%,

[1] If the distance r is taken as 1.2 × (the impeller diameter D_T) = 300 mm, say, and the largest significant forcing frequency is 700 Hz (the 6th harmonic for an impeller running at 1000 r.p.m.), then the largest wave number $k_{\max} \approx 2\pi \times 700\ \mathrm{Hz}/1400\ \mathrm{m\ s^{-1}} \approx 3.14\ \mathrm{m^{-1}}$, giving $(kr)_{\max} \approx 0.94$.

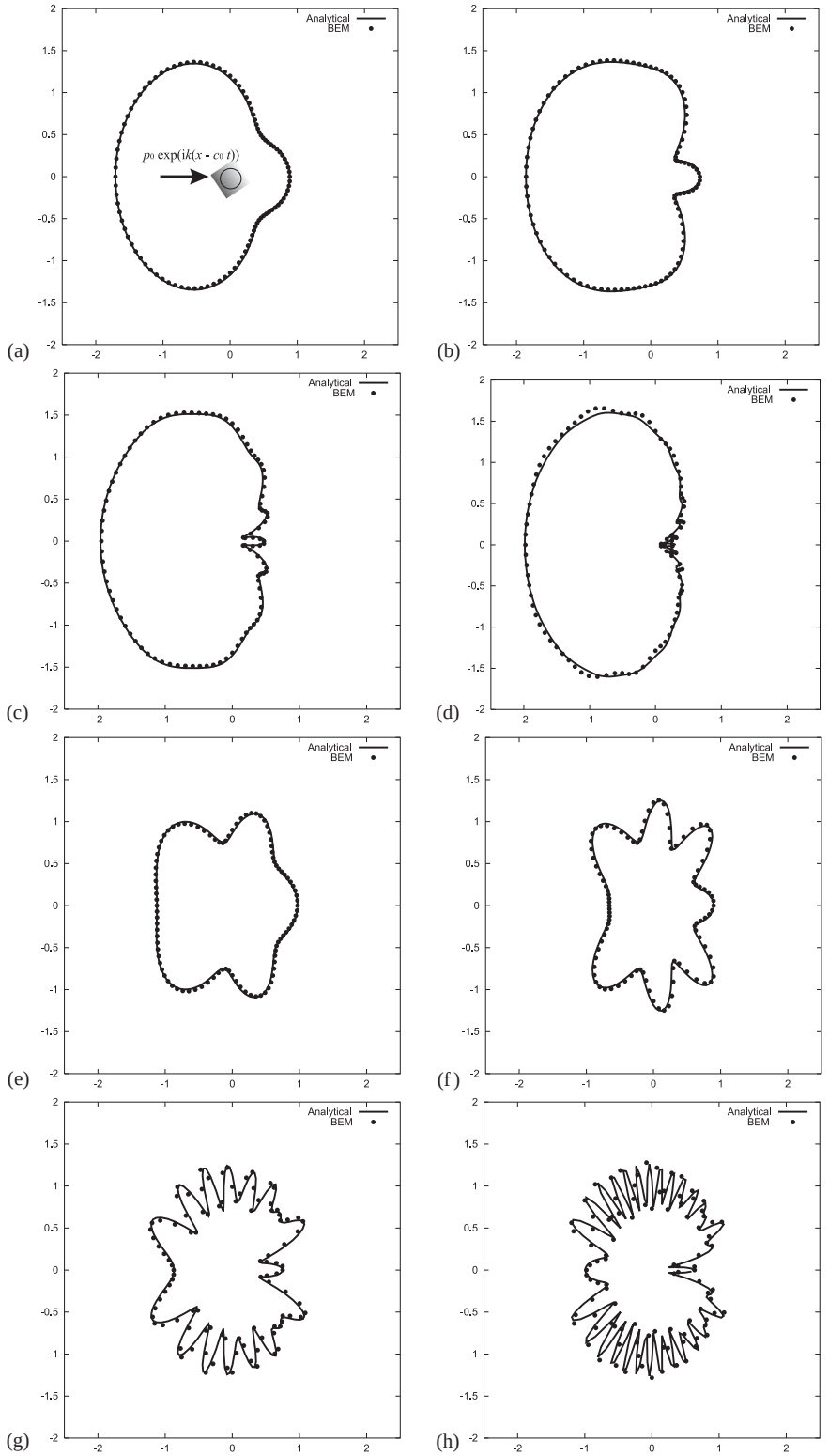

Fig. 3. Scattering of sound waves from a cylinder as a test case of the BEM. The cylinder has radius a, and its axis is in (0, 0). The incoming pressure wave is given by $p = p_0 \exp(\mathrm{i}k(x - c_0 t)) = p_0 \exp(\mathrm{i}k(r\cos\theta - c_0 t))$. The diagrams show the absolute pressure $|p/p_0|$ for various values of ka and r. Analytical results are depicted by full lines, and BEM calculations by dots. (a) $ka = 1, r = a$; (b) $ka = 2, r = a$; (c) $ka = 5, r = a$; (d) $ka = 10, r = a$; (e) $ka = 1, r = 5a$; (f) $ka = 2, r = 5a$; (g) $ka = 5, r = 5a$; (h) $ka = 10, r = 5a$.

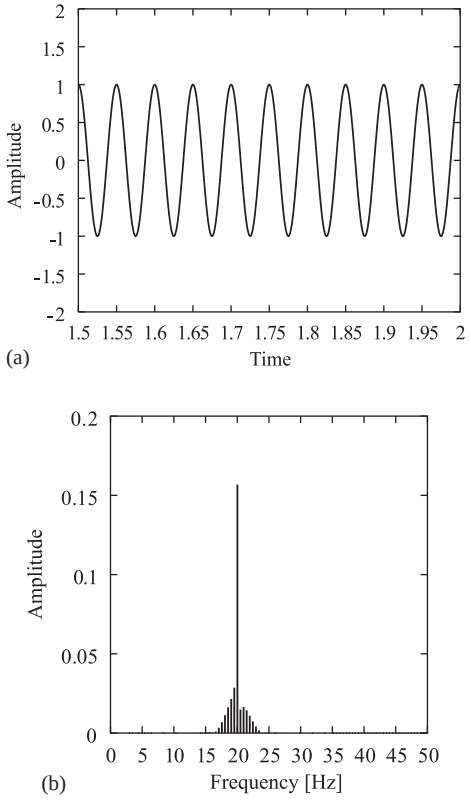

Fig. 4. (a) Time history of a point force placed at $\mathbf{y} = (0.5\text{ m}, 0)$; (b) Pressure spectrum at $\mathbf{x} = (0.5\text{ m}, 1.0\text{ m})$.

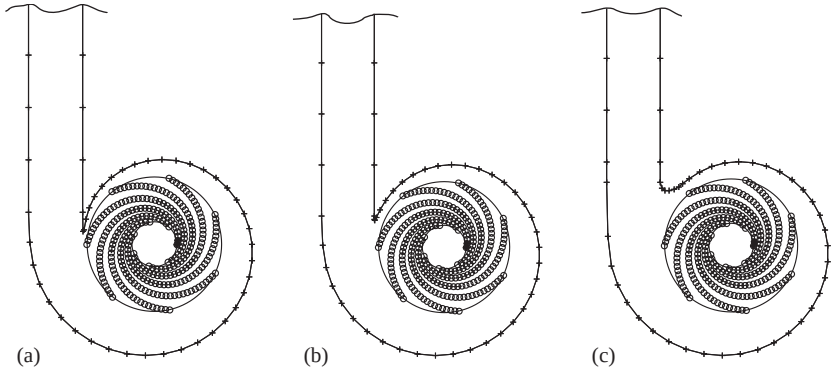

Fig. 5. Three different volute tongues. (a) Tongue 1; (b) Tongue 2; (c) Tongue 3.

respectively. Fig. 5 also indicates the distribution of the boundary element panels, and how many small panels are concentrated around the impeller tongue.

The acoustic pressure will be calculated at three points, A, B, and C, as illustrated by Fig. 6. Point A is very close to the impeller and the tongue. If the inlet source is placed at $(0, 0)$, point A is placed at the position $(-1.07R_T, 0.0)$. It corresponds to the placement of the pressure transducer E6 of Chu et al. (1995) and Dong et al. (1997). Point B is placed at the 'pump outlet', on the same height level as the upper part of the casing. Point C is placed 1 m away from point B, in the downstream direction. For tongue 1, the pressure will also be calculated at a point D, at $1.07R_T(\cos(192.4^\circ), \sin(192.4^\circ))$, which corresponds to the location of the pressure transducer E9 of Chu et al. (1995).

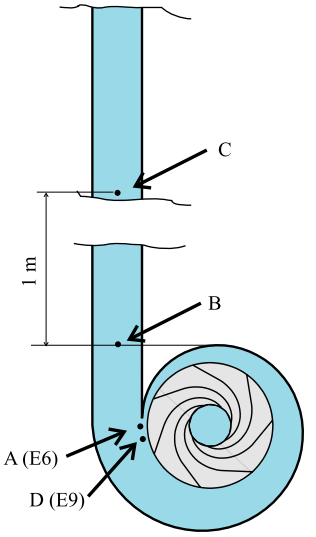

Fig. 6. Four locations for pressure calculations.

Table 1
Computational parameters

Number J of sampled force values in (27)	$2^{12} = 4096$
Number of point forces on each impeller blade	40
Number of elements on the pump casing	40
Number of elements on the exit pipe	40
Number of elements on the outer boundary	24

The discrete vortex computer program described in Part I was run to provide $J = 2^{12} = 4096$ force values in time for each of 40 control points on each impeller blade, for each of the three volute tongues. The computational parameters for the acoustic analysis is given in Table 1.

5.2. On the accuracy of the analysis

With 40 elements on the pump casing, the length of the largest element is 0.047 m. With also 40 elements on the exit channel, the element length there is 0.095 m. With a pump speed of 890 r.p.m. the blade passage frequency f_{blade} is 103.8 Hz. With $c_0 = 1400$ m s^{-1} the acoustic wavelength of the nth harmonic is $\lambda = c_0/(nf_{\text{blade}}) = 13.5/n$ m. The exit channel is thus covered with $141/n$ panels per wavelength. A common 'rule-of-thumb' in solution of acoustic (and other wave-type) problems with the finite element method is that the element length should be less than $\frac{1}{10}$th of the minimum wavelength [e.g. Zienkiewicz (2000)]. Applying this rule here, the present discretization should provide sufficient accuracy up to the 14th harmonic, although we will, at most, be interested only in the first six. Another recommendation, related directly to the boundary element method, is that nodal distances should be smaller than the speed of sound c_0 times the simulation time step Δt (Wells and Renaut, 1997). The time step used to generate the blade force time series is $\Delta t = 3.75 \times 10^{-4}$ s. This gives $c_0 \Delta t \approx 0.52$ m which indeed is larger than the largest element.

Returning to the verification test illustrated by Fig. 3 (Section 4), it is noted that the 'high-frequency case' of $ka = 10$ corresponds to an acoustic wavelength of $\lambda = 2\pi a/10$. As the cylinder of radius a is covered with 100 panels, the length of each panel is $2\pi a/100$, that is, exactly $\frac{1}{10}$th of the minimum wavelength considered. The results of Fig. 3 appear to verify that the mentioned finite element 'rule-of-thumb' applies to the boundary element method as well.

The analysis to follow will make of a pressure level PL, defined as

$$PL(\mathbf{x}, \omega) = 20 \log_{10}(|p(\mathbf{x}, \omega)|/p_0) \quad (\text{dB}), \quad p_0 = \tfrac{1}{2} \rho_0 U_T^2. \tag{35}$$

Fig. 7 illustrates the convergence of (35) at the blade passage frequency f_{blade}, at the two points A and C. The shown quantity is the error in the pressure level obtained with N elements, relative to the result with (a chosen value of) 100 elements. In contrast to the discussion above, use of just 40 panels on either casing or exit channel may appear too

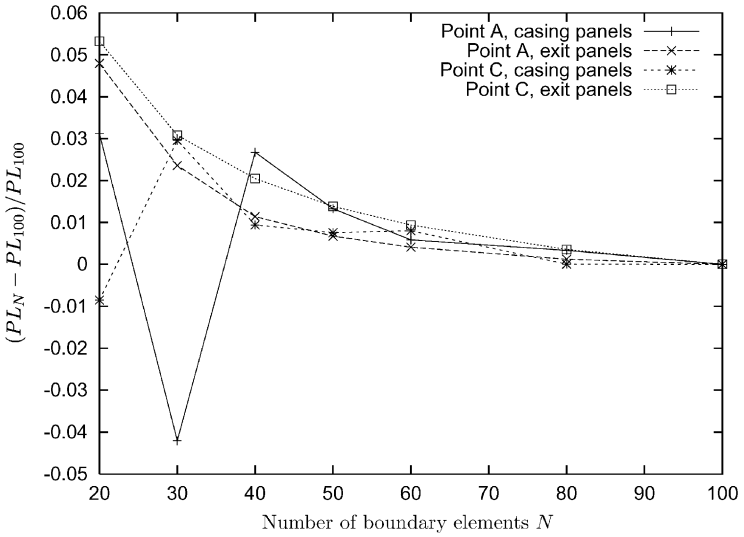

Fig. 7. Convergence of the pressure level PL (as defined by (35)) at the blade passage frequency f_{blade}, at two different points (A and C). PL_N stands for the pressure level with N boundary elements (and PL_{100} is with 100 elements). When the number of casing (exit) panels is changed the number of exit (casing) panels is kept constant equal to 40 panels.

coarse. However the error, relative to the 100 panel solution, is below 3% in any case. It is noted that the convergence is approximately linear in the range $40 \leqslant N < 100$. To limit the computational demands, the analysis to follow will be carried out with 40 elements on both casing and exit channel.

It was verified in Part I that changing the number of dipoles on the impeller blades from 20 to 40 does not significantly alter velocity and pressure difference across the blades at the most downstream control points. It appears thus that 40 dipoles per blade gives a satisfactory representation, and the effect of dipoles density on the pressure levels will not be further analyzed here.

5.3. Results of calculations and comparison with experimental results

Figs. 8(a), (b) shows the pressure spectra at points A and D. The results of the present analysis are shown by the 'impulses' while the experimental results of Chu et al. (1995) (their Fig. 10, with reference pressure 1 μPa converted to $\frac{1}{2}\rho_0 U_T^2$) are represented by dots. The 'thickness' of the impulses is because not only the frequencies nf_{blade}, $n = 1, 2, \ldots, 6$, were analyzed, but also the frequencies corresponding to the nearest four surrounding 'bins', in order to verify that the peaks actually are at nf_{blade}. More precisely, the following frequency composants are shown:

$$f = nf_{\text{blade}} + m\Delta f, \quad n = 1, 2, \ldots, 6, \quad m = -2, -1, \ldots, 2, \tag{36}$$

where $\Delta f = 1/J\Delta t$. It is a general trend that the numerical pressures are somewhat higher than the experimental ones. But an overestimation of the pressure by the two-dimensional model is to be expected because, in reality, the pressure fluctuations will be reduced by leakage flow and three-dimensional effects due to rounding-off of the tongue, etc. The general characteristics of the frequency spectra are seen to be captured well. The presence of harmonics of the blade passage frequency is because the pressure signature is harmonic but not pure sinuous. Domination of the second harmonic $2f_{\text{blade}}$ over the fundamental frequency f_{blade}, as in Fig. 8(b), has also been found experimentally by Chu et al. (1995), but at a slightly different location, namely at $1.07R_T(\cos(198.8^\circ), \sin(198.8^\circ))$, at their pressure transducer E10. Guelich and Bolleter (1992) show a similar example, and point out that the second harmonic often comes out strongly.

It appears that the balance between the fundamental blade passage frequency and its harmonics depends on the position of measurement/calculation is a complicated way. As to the experimental system, the pump diffuser, through which the exit gradually changes from square to circular shape, might have some influence of this balance. So may also the following piping, although Chu et al. (1995) took care to eliminate reflections therefrom, by connecting the pump exit and the piping via a spiralled-up rubber hose. These effects are, unfortunately, difficult to represent well in the present numerical model, but future numerical investigations of the effects of exit (diffusor) geometry might be useful.

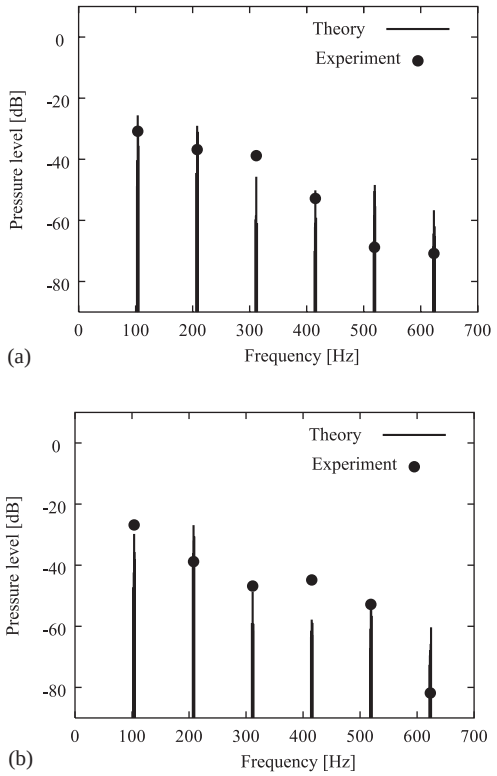

Fig. 8. (a) Pressure spectrum at point D. Comparison between present numerical results (impulses) and the experimental results (dots) of Chu et al. (1995), corresponding to their point E9; (b) The same at point A, corresponding to point E6 of Chu et al. (1995).

Fig. 9 illustrates the influence of tongue geometry on the pressure levels at the three points A, B, and C. At point C, the pressure level for f_{blade} decreases approximately 1.4 dB by changing from tongue 1 to 2. The experimental result (Dong et al., 1997) is 5 dB. The change from tongue 1 to 3 results in a decrease in the calculated pressure level for f_{blade} by approximately 16 dB, where the experimental value is about 10 dB.

By comparison with Fig. 8 it is seen that the pressure level for tongue 1 at f_{blade} decreases by approximately 6 dB (i.e. halving of the pressure amplitude) when moving from point D to C. By comparing the power spectra in Chu et al. (1995) with those in Dong et al. (1997) it is seen that the corresponding experimental pressure level decreases by about 7.5 dB.

The influence of reduced pump speed and reduced flow rate was also considered for the blade passage frequency, at point C. Reducing the pump speed from 890 to 600 r.p.m., and keeping the flow rate constant (source strength kept at 0.675 $\text{m}^2\ \text{s}^{-1}$) resulted in a pressure level reduction of about 15 dB. Reducing the flow rate by changing the source strength to 0.5 $\text{m}^2\ \text{s}^{-1}$, and keeping the pump speed at 890 r.p.m., did not imply any significant change in pressure level.

As discussed in Section 1, the dipole-type flow noise is mainly generated by the oscillating surface pressures which reach a maximum when the flow from the fluid channel between to impeller blades is blocked by the volute tongue. Fig. 10 depicts the oscillating fluid force at the most downstream control point of one of the impeller blades, for the three different tongues, and illustrates how the force amplitude decreases by increasing gap.

6. Minimization of flow-induced noise by optimization of the tongue geometry

One of the greatest advantages of the frequency-domain solution (19) of the acoustic pressure is in connection with minimization of the flow-noise by design optimization, for example by optimizing the tongue geometry. As discussed earlier, the dominating pressure components are located at the blade passage frequency f_{blade} and its harmonics, $2f_{\text{blade}}$,

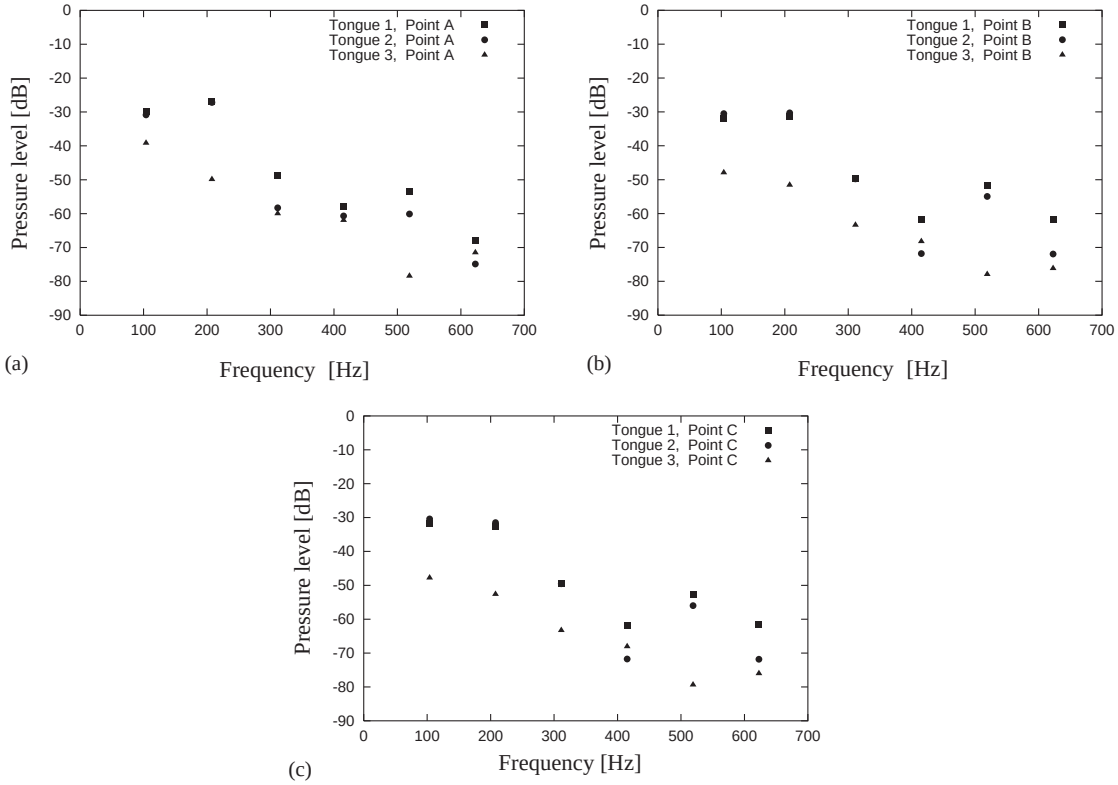

Fig. 9. Comparison of pressure levels for three different volute tongues. (a) At point A; (b) At point B; (c) At point C.

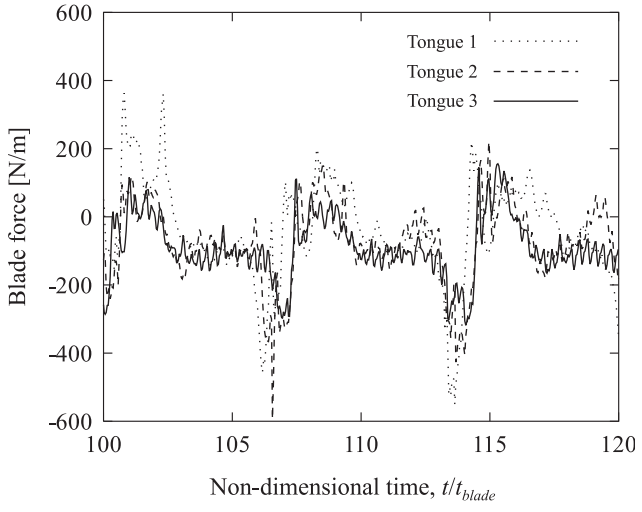

Fig. 10. Blade force at the most downstream control point, for three different volute tongues.

$3f_{\text{blade}}, \ldots$. The aim may then be to determine the shape of the volute tongue which minimizes the largest frequency composant of the pressure at a given position $\mathbf{x}_*$. A numerical method will be outlined in the following. (A numerical example has been reported in Langthjem and Olhoff, 2001.)

As described in Part I, the tongue design is described by a B-spline curve,

$$\mathscr{F} = \mathscr{F}(\mathbf{x}_1(d_1), \mathbf{x}_2(d_2) \ldots) \tag{37}$$

say, where $\mathbf{x}_1, \mathbf{x}_2, \ldots$ are a few control points which locations are controlled by the scalar design variables $d_1, d_2, \ldots$ (the points are to be moved along specified lines). A mathematical optimization problem may be defined as follows:

$$\min_{\mathscr{F} \in \{\mathscr{F}_d\}} \max_i |p_i(\mathbf{x}_*, \omega_i)|, \tag{38}$$

where $\{\mathscr{F}_d\}$ represents the admissible design space. Eq. (38) may be converted into a pure min-problem by defining an additional design variable, $p_{\max}$:

$$\begin{aligned} &\min \quad p_{\max} \\ &\text{s.t.} \quad \text{(i)} \ p_{\max} \geqslant |p_1(\mathbf{x}_*, \omega_1)|, |p_2(\mathbf{x}_*, \omega_2)|, \ldots, \\ &\qquad \text{(ii)} \ \underline{d} \leqslant d_j \leqslant \bar{d}, \quad j = 1, 2, \ldots \ . \end{aligned} \tag{39}$$

Here $\underline{d}$ and $\bar{d}$ are lower and upper bounds on the design variables. The nonlinear constraints (i) may be linearized such that the optimization problem can be solved iteratively, for example by sequential linear programming. For the $(k+1)$th optimal redesign problem, the linearized constraints (i) take the form

$$p_{\max} \geqslant |p_i^{k+1}| \approx |p_i^k| + \sum_j \frac{\partial |p_i^k|}{\partial d_j} \Delta d_j, \quad i = 1, 2, \ldots \ . \tag{40}$$

The frequency-domain solution (19) provides a basis for efficient evaluation of the dominating noise components. The fluid forces $\mathbf{f}_n(\mathbf{y}_n(t), t)$ are also affected by the design changes, but numerical tests have shown that the influence is small for 'moderate' design changes. By significant remodelling of the tongue shape, the fluid forces have to be reevaluated during the design iterations.

Differentiation of $p_* = p(\mathbf{x}_*, \omega)$ (Eq. (31)) with respect to the design parameter d_j gives

$$\frac{\partial p_*}{\partial d_j} = \frac{\partial \mathbf{s}_*^{\mathrm{T}}}{\partial d_j} \mathbf{p}_s + \frac{\partial \mathbf{p}_s}{\partial d_j} \mathbf{s}_*^{\mathrm{T}}, \tag{41}$$

using that $\partial \mathbf{q}_* / \partial d_i = 0$ as $\mathbf{q}_*$ is held constant (in accordance with the discussion above). The vector $\partial \mathbf{p}_s / \partial d_j$ can be obtained by differentiation of (30) as

$$\frac{\partial \mathbf{p}_s}{\partial d_j} = \left[\frac{1}{2} \mathbf{I} - \mathbf{S}_0 \right]^{-1} \frac{\partial \mathbf{S}_0}{\partial d_j} \mathbf{p}_s, \tag{42}$$

using that $\partial \mathbf{q}_0 / \partial d_i = 0$.

7. Conclusion

This paper has described a two-dimensional numerical method for estimating the acoustic pressure fluctuations in a centrifugal pump, due to the unsteady surface forces which act as acoustic dipoles. In the example considered, the estimates of the strengths of the dipoles rely on the discrete vortex method (DVM). DVM gives the velocity field, whereafter the pressure on the blades is evaluated by applying the unsteady Bernoulli equation. The unsteady pressure on the volute also acts as distributed dipole sources whose strengths are determined by applying the BEM.

The use of DVM is just one possible method of estimating the dipole strengths. Alternatively, commercial or 'in-house' computational fluid dynamics (CFD) codes (based on finite or boundary elements, or finite difference) may be used to provide this data.

Solution (27) to the inhomogeneous wave equation (4) is determined directly in the frequency domain. Similar solutions are given by Lockard (2000) and Guo (2000). Both papers consider problems with a single moving body in otherwise unbounded space, such that the solutions can be conveniently expressed in moving coordinate systems. The rotor–stator interaction problem of the present paper is more complicated, and it is of little help to consider a coordinate system moving with the impeller, as the volute then will be rotating in that system. Thus, the positions of the dipoles need to be updated at every time step, as expressed by (27). This equation may, we hope, also be useful for estimating noise generation in other types of machinery with rotor–stator interaction.

The present numerical procedure has been checked by comparing the numerical results with available experimental data. Better agreement between theory and experiment than found here has been reported for both unducted and ducted air-conveying centrifugal fans (Jeon and Lee, 1999, 2000). But the water-conveying centrifugal pump may be a 'harder' problem, for the following reasons. The sound (compression) waves move much faster in water than in air (1400 versus 340 m s^{-1}). Furthermore, the attenuation of the sound waves is weaker in water than in air, as the kinematic viscosity is smaller (1.00×10^{-6} versus 15.1×10^{-6} m^2 s^{-1}, at 20°C). Disturbances and reflections may thus

interfere stronger in a pump, making both experimental and numerical analyses more difficult than by a fan. Some neglected details in the numerical model, such as reflections from the impeller hub, may then have influence on the results. This could be included in future studies. A better representation of the impeller blades, by distributed forces (dipoles) rather than concentrated (lumped) ones, can also be suggested as a point of improvement.

In conclusion, although a better agreement between theory and experiment could be wished for, we feel that the presented results support the initial assumptions that:

(i) the sound generated in the centrifugal pump is determined mainly by the unsteady surface forces;
(ii) the discrete vortex method can provide a sufficiently accurate estimate of these forces;
(iii) a two-dimensional analysis is capable of capturing the basic features of acoustic pressure fluctuations in a flat, 'two-dimensional' laboratory centrifugal pump.

Acknowledgements

Financial support from Aalborg University, Grundfos A/S, the Alexander von Humbolt Foundation, and the Danish Ministry of Research is gratefully acknowledged. We are most grateful for the helpful discussions with A. Back-Pedersen, K.S. Dahl, C.B. Jacobsen and J.B. Nielsen of Grundfos A/S. Helpful suggestions by Professor D.S. Weaver are gratefully acknowledged. We also wish to thank the referees for many helpful suggestions to improve the paper. The first author (M.L.) would finally like to thank Professors H. Umemiya and M. Nakano at Yamagata University for the opportunity to complete this work.

Appendix A. Extension to three dimensions

In changing the solution (19) to one valid in three dimensions we return to the general solution (10). The three-dimensional Green's function is, in terms of its Fourier transform, given by (Howe, 1998)

$$G(x,y,t,\tau)=\frac{1}{8\pi^2c_0^2}\int_\omega \frac{\mathrm{e}^{\mathrm{i}kr(\tau)}}{r(\tau)}\mathrm{e}^{-\mathrm{i}\omega t}\mathrm{e}^{\mathrm{i}\omega\tau}\,\mathrm{d}\omega. \tag{A.1}$$

The forces $\mathbf{f}_n$ are now to be considered as point forces, not as line forces. They are obtained as pressure difference Δp_n (at blade control point n) times the area A_n of impeller blade panel n. The three-dimensional version of the frequency-domain solution (19) takes the form

$$\begin{aligned} c(\mathbf{x})p(\mathbf{x},\omega)=&\frac{1}{4\pi}\sum_{n=1}^{N_f}\int_\tau \mathbf{f}_n(\mathbf{y}_n(\tau),\tau)\cdot\frac{\partial}{\partial\mathbf{y}}\left(\frac{\mathrm{e}^{\mathrm{i}kr_n(\tau)}}{r_n(\tau)}\right)\mathrm{e}^{\mathrm{i}\omega\tau}\,\mathrm{d}\tau\\ &+\frac{1}{4\pi}\int_S p(\mathbf{y}_s,\omega)\frac{\partial}{\partial\mathrm{n}}\left(\frac{\mathrm{e}^{\mathrm{i}kr_S}}{r_S}\right)\mathrm{d}S, \end{aligned} \tag{A.2}$$

where the result used to obtain (20) also has been implemented. The derivatives of the function $\mathrm{e}^{\mathrm{i}kr}/r$ are given by

$$\begin{aligned} \frac{\partial}{\partial y_\alpha}\left(\frac{\mathrm{e}^{\mathrm{i}kr_n}}{r_n}\right)&=\left\{\frac{1}{r_n^3}-\frac{\mathrm{i}k}{r_n^2}\right\}(x_\alpha-y_{\alpha n})\,\mathrm{e}^{\mathrm{i}kr_n},\\ \frac{\partial}{\partial\mathrm{n}}\left(\frac{\mathrm{e}^{\mathrm{i}kr_S}}{r_S}\right)&=\left\{\frac{1}{r_S^3}-\frac{\mathrm{i}k}{r_S^2}\right\}(\mathbf{x}-\mathbf{y}_S)\cdot\mathbf{n}\mathrm{e}^{\mathrm{i}kr_S}. \end{aligned} \tag{A.3}$$

References

Abramowitz, M., Stegun, I.A., 1972. Handbook of Mathematical Functions. Dower, New York.

Chen, G., Zhou, J., 1992. Boundary Element Methods. Academic Press, London.

Chu, S., Dong, R., Katz, J., 1995. Relationship between unsteady flow, pressure fluctuations, and noise in a centrifugal pump—Parts A and B. ASME Journal of Fluids Engineering 117, 24–35.

Crighton, D.G., Dowling, A.P., Ffowcs Williams, J.E., Heckl, M., Leppington, F.G., 1992. Modern Methods in Analytical Acoustics. Springer, London.

Curle, N., 1955. The influence of solid boundaries upon aerodynamic sound. Proceedings of the Royal Society A 231, 505–514.
Dong, R., Chu, S., Katz, J., 1997. Effect of modification to tongue and impeller geometry on unsteady flow, pressure fluctuations, and noise in a centrifugal pump. ASME Journal of Fluids Engineering 119, 506–515.
Farassat, F., Brentner, K.S., 1998. The acoustic analogy and the prediction of the noise of rotating blades. Theoretical and Computational Fluid Dynamics 10, 155–170.
Ffowcs Williams, J.E., Hawkings, D.L., 1969a. Theory relating to the noise of rotating machinery. Journal of Sound and Vibration 10, 10–21.
Ffowcs Williams, J.E., Hawkings, D.L., 1969b. Sound generation by turbulence and surfaces in arbitrary motion. Philosophical Transactions of the Royal Society A 264, 321–342.
Guelich, J.F., Bolleter, U., 1992. Pressure pulsations in centrifugal pumps. ASME Journal of Vibration and Acoustics 114, 272–279.
Guo, Y.P., 2000. Application of the Ffowcs Williams/Hawkings equation to two-dimensional problems. Journal of Fluid Mechanics 403, 201–221.
Hansen, E.B., 1991. Partielle Differentialligninger (Partial Differential Equations. Lecture Notes). Laboratory for Applied Mathematical Physics, Technical University of Denmark (in Danish).
Howe, M.S., 1991. On the estimation of sound produced by complex fluid-structure interactions, with application to a vortex interacting with a shrouded rotor. Proceedings of the Royal Society A 433, 573–598.
Howe, M.S., 1998. Acoustics of Fluid–Structure Interaction. Cambridge University Press, Cambridge.
Jeon, W.-H., Lee, D.J., 1999. An analysis of the flow and aerodynamic acoustic sources of a centrifugal impeller. Journal of Sound and Vibration 222, 505–511.
Jeon, W.-H., Lee, D.J., 2000. An analysis of generation and radiation of sound for a centrifugal fan. In: Proceedings of the Seventh International Congress of Sound and Vibration 2000, Garmisch-Partenkirchen, pp. 1235–1242.
Langthjem, M.A., Olhoff, N., 2001. Optimum design of the volute tongue against flow-induced noise in a centrifugal pump. In: Proceedings of the Fourth World Congress of Structural and Multidisciplinary Optimization (CD-ROM), Dalian, China, June 4–8, 2001, 6pp.
Langthjem, M.A., Olhoff, N., 2003. A numerical study of flow-induced noise in a centrifugal pump. Part I. Hydrodynamics. Journal of Fluids and Structures, this volume, doi:10.1016/j.jfluidstructs.2004.01.003.
Lighthill, M.J., 1952. On sound generated aerodynamically. I. General theory. Proceedings of the Royal Society A 211, 564–587.
Lighthill, M.J., 1962. The Bakerian lecture, 1961. Sound generated aerodynamically. Proceedings of the Royal Society A 267, 147–182.
Lighthill, J., 1978. Waves in Fluids. Cambridge University Press, Cambridge.
Lockard, D.P., 2000. An efficient, two-dimensional implementation of the Ffowcs Williams and Hawkings equation. Journal of Sound and Vibration 229, 897–911.
Lowson, M.V., 1965. The sound field for singularities in motion. Proceedings of the Royal Society A 286, 559–572.
Morse, P.M., Ingard, K.U., 1986. Theoretical Acoustics. Princeton University Press, Princeton.
Press, W.H., Teukolsky, S.A., Vetterling, W.T., Flannery, B.P., 1992. Numerical Recipes in FORTRAN. The Art of Scientific Computing. Cambridge University Press, Cambridge.
Rzentkowski, G., 1996. Generation and control of pressure pulsations emitted from centrifugal pumps: a review. In: Proceedings of Flow-Induced Vibrations 1996, Montreal, pp. 439–454.
Wells, V.L., Renaut, R.A., 1997. Computing aerodynamically generated noise. Annual Review of Fluid Mechanics 29, 161–199.
Wu, T.W., Wan, G.C., 1992. Numerical modeling of acoustic radiation and scattering from thin bodies using a Cauchy principal integration equation. Journal of the Acoustic Society of America 92, 2900–2906.
Zienkiewicz, O.C., 2000. Achievements and some unsolved problems of the finite element method. International Journal for Numerical Methods in Engineering 47, 9–28.